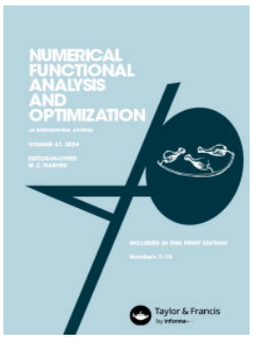

Taylor & Francis
Taylor & Francis Group

Numerical Functional Analysis and Optimization

ISSN: 0163-0563 (Print) 1532-2467 (Online) Journal homepage: www.tandfonline.com/journals/lnfa20

Numerical Analysis for the Normalized Time-Fractional Modica–Mortola Functional

Zhengang Li , Soobin Kwak , Xinpei Wu , Juho Ma , Qunzhi Jin & Junseok Kim

To cite this article: Zhengang Li , Soobin Kwak , Xinpei Wu , Juho Ma , Qunzhi Jin & Junseok Kim (22 Jul 2026): Numerical Analysis for the Normalized Time-Fractional Modica–Mortola Functional, Numerical Functional Analysis and Optimization, DOI: 10.1080/01630563.2026.2696795

To link to this article: https://doi.org/10.1080/01630563.2026.2696795

NUMERICAL FUNCTIONAL ANALYSIS AND OPTIMIZATION
https://doi.org/10.1080/01630563.2026.2696795

Numerical Analysis for the Normalized Time-Fractional Modica–Mortola Functional

Zhengang Li[a], Soobin Kwak[a], Xinpei Wu[a], Juho Ma[a], Qunzhi Jin[b], and Junseok Kim[a]

[a]Department of Mathematics, Korea University, Seoul, Republic of Korea; [b]College of Science, Yanbian University, Yanji, China

ABSTRACT

In this work, we study the gradient flow of the normalized time-fractional Modica–Mortola (MM) functional and propose a numerical method combining operator splitting with finite differences, where an analytical solution is used for the nonlinear reaction term to capture the memory effects inherent in fractional dynamics. Numerical experiments show the effect of the normalized fractional order on interface evolution. The results indicate that the normalized time-fractional MM functional allows flexible control of interfacial dynamics through the fractional order and provides a numerical method for simulating fractional phase-field models.

ARTICLE HISTORY
Received 30 October 2025
Revised 2 June 2026
Accepted 25 June 2026

KEYWORDS
Time-fractional; Modica–Mortola functional; phase-field model

1. Introduction

The phase-field model is a computational approach that describes interface evolution using continuous field variables, which avoids explicit interface tracking by introducing a phase-field function. It is widely applied in materials science for crystal growth [1,2] and phase transition simulations [3,4], as well as in fluid dynamics for multiphase flows [5,6] and interface dynamics [7]. Building on these fundamentals, recent studies continue to expand its application scope and improve model performance. Wang et al. [8] used a phase-field multiphase-flow model with a modified ensemble Kalman filter and adaptive ensembles to assimilate information and improve state estimation accuracy. Lai et al. [9] used a phase-field framework with dual-energy physics-informed topology optimization to design multi-material layouts and achieved improved performance and manufacturability. Li et al. [10] used an unconditionally stable phase-field model for ternary systems with liquid–solid transition to capture robust multi-component evolution without stability-induced time-step restrictions. Xia et al. [11] used phase-field Allen–Cahn (AC) analysis on non-uniform cell sizes to improve numerical accuracy and stability across heterogeneous meshes.

The Modica–Mortola (MM) functional provides a variational method for phase-field models by combining gradient terms with a potential energy term.

CONTACT Junseok Kim cfdkim@korea.ac.kr Department of Mathematics, Korea University, Seoul 02841, Republic of Korea.

Unlike the classical AC equation, which is based on a double-well potential and thus restricted to two stable phases ($\phi = \pm 1$), the MM functional uses a periodic multi-well potential, such as $\sin^2(\pi\phi)/\epsilon$, so that every integer value of ϕ represents a stable phase. This enables the MM approach to naturally capture the evolution of multiphase systems and makes it suitable for problems involving complex phase interactions beyond binary settings. Giga et al. [12] provided explicit representations of the Kobayashi–Warren–Carter energy and the Gamma limit of a single-well MM functional in one dimension, established compactness under graph convergence, and introduced a new method of unfolding by the arc-length parameter.

Time-fractional models [13–16] introduce fractional time derivatives to capture memory effects and nonlocal dynamics, which are widely used in phase-field modeling of phase transition processes [17–19]. Wang et al. [20] proposed a fast finite element BiCG algorithm for the fractional Cahn–Hilliard (CH) equation that preserves energy dissipation. The normalized time-fractional formulation [21] introduces a fractional derivative in time that is scaled to ensure proper normalization of the kernel, which avoids artificial damping or amplification of the solution. Wang et al. [22] introduced a normalized time-fractional AC model and demonstrated that normalization yields a unique time scale and allows parameter-based control of the evolution. Lee et al. [23] proposed a time-fractional CH formulation with a normalized derivative, solved *via* a Fourier spectral technique, and demonstrated that the approach effectively captures phase separation dynamics and allows consistent comparison across fractional orders. We present a time-fractional MM functional based on a normalized derivative:

$$\frac{\partial^\alpha \phi(\mathbf{x},t)}{\partial t^\alpha} = -\frac{\pi}{\epsilon}\sin\big(2\pi\phi(\mathbf{x},t)\big) + 2\epsilon\Delta\phi(\mathbf{x},t), \tag{1}$$

$$\mathbf{n}\cdot\nabla\phi = 0 \text{ on } \partial\Omega, \tag{2}$$

where ϵ controls the thickness of the interfacial layer, $\phi(\mathbf{x},t)$ denotes the order parameter defined on $\mathbf{x} \in \Omega$ and time t, and $\mathbf{n}$ represents the outward unit normal vector on $\partial\Omega$.

$$\frac{\partial^\alpha \phi(\mathbf{x},t)}{\partial t^\alpha} = \frac{1-\alpha}{t^{1-\alpha}}\int_0^t \frac{\partial\phi(\mathbf{x},s)}{\partial s}\frac{ds}{(t-s)^\alpha}, \quad 0<\alpha<1. \tag{3}$$

This definition satisfies the normalization condition:

$$\frac{1-\alpha}{t^{1-\alpha}}\int_0^t \frac{ds}{(t-s)^\alpha} = 1, \quad 0<\alpha<1. \tag{4}$$

Equation (1) represents the gradient flow associated with the MM functional:

$$\mathcal{E}(\phi) := \int_\Omega \left[\frac{1}{\epsilon}\sin^2(\pi\phi) + \epsilon|\nabla\phi|^2\right] d\mathbf{x}. \tag{5}$$

Here, $(1/\epsilon)\sin^2(\pi\phi)$ defines the multi-well potential, as illustrated in Figure 1.

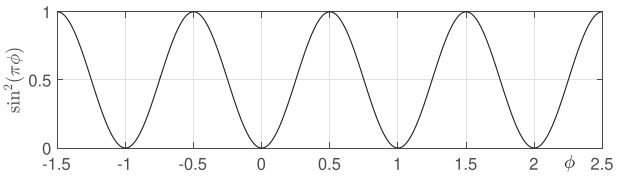

Figure 1. $\sin^2(\pi\phi)$ on $[-1.5,\ 2.5]$.

The paper is organized as follows. In Section 2, the computational solution algorithm is described. In Section 3, the numerical tests are presented. In Section 4, the conclusions are given.

2. Numerical solution algorithm

Consider the computational domain $\Omega = (L_x, R_x) \times (L_y, R_y)$ and use a uniform cell-centered mesh with spacing $h = (R_x - L_x)/N_x$. The grid points are defined by $(x_i, y_j) = \left(\left(i - \frac{1}{2}\right)h + L_x,\ \left(j - \frac{1}{2}\right)h + L_y\right)$, for $i = 1, \ldots, N_x$ and $j = 1, \ldots, N_y$. Let ϕ_{ij}^n denote the numerical approximation of $\phi(x_i, y_j, t_n)$ at the time level $t_n = (n-1)\Delta t$. The normalized time-fractional derivative at $t = t_{n+1}$ can be approximated as follows [24]:

$$
\begin{aligned}
\frac{\partial^\alpha \phi(x_i, y_j, t_{n+1})}{\partial t^\alpha} &= \frac{1-\alpha}{t_{n+1}^{1-\alpha}} \sum_{p=1}^{n} \int_{t_p}^{t_{p+1}} \frac{\partial \phi(x_i, y_j, s)}{\partial s} \frac{ds}{(t_{n+1} - s)^\alpha} \\
&= \sum_{p=1}^{n} \frac{1-\alpha}{t_{n+1}^{1-\alpha}} \int_{t_p}^{t_{p+1}} \frac{ds}{(t_{n+1} - s)^\alpha} \left(\frac{\phi_{ij}^{p+1} - \phi_{ij}^{p}}{\Delta t} + O(\Delta t) \right) \\
&= \sum_{p=1}^{n} \frac{(n+1-p)^{1-\alpha} - (n-p)^{1-\alpha}}{n^{1-\alpha}} \left(\frac{\phi_{ij}^{p+1} - \phi_{ij}^{p}}{\Delta t} + O(\Delta t) \right) \\
&= \sum_{p=1}^{n} w_p^n \left(\frac{\phi_{ij}^{p+1} - \phi_{ij}^{p}}{\Delta t} + O(\Delta t) \right) \\
&= w_n^n \left(\frac{\phi_{ij}^{n+1} - \phi_{ij}^{n}}{\Delta t} + O(\Delta t) \right) + \sum_{p=1}^{n-1} w_p^n \left(\frac{\phi_{ij}^{p+1} - \phi_{ij}^{p}}{\Delta t} + O(\Delta t) \right) \\
&= w_n^n \frac{\partial \phi(x_i, y_j, t_{n+1})}{\partial t} + \sum_{p=1}^{n-1} w_p^n \frac{\phi_{ij}^{p+1} - \phi_{ij}^{p}}{\Delta t} + O(\Delta t), \qquad (6)
\end{aligned}
$$

where $w_p^n = [(n+1-p)^{1-\alpha} - (n-p)^{1-\alpha}]/n^{1-\alpha}$ and $\sum_{p=1}^{n} w_p^n = 1$. We then rewrite the normalized time-fractional MM functional as the following approximation equation:

$$\frac{\partial \phi(x_i, y_j, t_{n+1})}{\partial t} = -\frac{\pi \sin(2\pi(\phi(x_i, y_j, t_{n+1})))}{w_n^n \epsilon} + \frac{2\epsilon}{w_n^n}\Delta\phi(x_i, y_j, t_{n+1}) - \frac{1}{w_n^n}\sum_{p=1}^{n-1} w_p^n \frac{\phi_{ij}^{p+1} - \phi_{ij}^p}{\Delta t}. \tag{7}$$

To solve equation (1) numerically, we apply the operator splitting method (OSM), expressed as:

$$\textbf{Step 1}: \quad \frac{\partial \phi(x_i, y_j, t_{n+1})}{\partial t} = -\frac{\pi \sin(2\pi(\phi(x_i, y_j, t_{n+1})))}{w_n^n \epsilon}. \tag{8}$$

$$\textbf{Step 2}: \quad \frac{\partial \phi(x_i, y_j, t_{n+1})}{\partial t} = \frac{2\epsilon}{w_n^n}\phi_{xx}(x_i, y_j, t_{n+1}) - \frac{1}{2w_n^n}\sum_{p=1}^{n-1} w_p^n \frac{\phi_{ij}^{p+1} - \phi_{ij}^p}{\Delta t}. \tag{9}$$

$$\textbf{Step 3}: \quad \frac{\partial \phi(x_i, y_j, t_{n+1})}{\partial t} = \frac{2\epsilon}{w_n^n}\phi_{yy}(x_i, y_j, t_{n+1}) - \frac{1}{2w_n^n}\sum_{p=1}^{n-1} w_p^n \frac{\phi_{ij}^{p+1} - \phi_{ij}^p}{\Delta t}. \tag{10}$$

For **Step 1**, we use an analytical solution to solve it, as follows. The detailed derivation process can be found in [25].

$$\phi_{ij}^* = \left\lfloor \phi_{ij}^n \right\rfloor + \frac{1 + \operatorname{sgn}(\bar{\phi}_{ij}^n - 0.5)}{2} + \frac{\operatorname{sgn}\left(0.5 - \bar{\phi}_{ij}^n\right)}{2\pi} \cos^{-1}\left(\frac{1 - e^{-\frac{4\pi^2}{w_n^n \epsilon}\Delta t + 4\pi I_{ij}^n}}{1 + e^{-\frac{4\pi^2}{w_n^n \epsilon}\Delta t + 4\pi I_{ij}^n}}\right), \tag{11}$$

where

$$I_{ij}^n = \frac{1}{4\pi} \ln \frac{1 - \cos\left(2\pi\phi_{ij}^n\right)}{1 + \cos\left(2\pi\phi_{ij}^n\right)} \quad \text{and} \quad \bar{\phi}_{ij}^n = \phi_{ij}^n - \left\lfloor \phi_{ij}^n \right\rfloor.$$

We define $\operatorname{sgn}(x)$ as the sign function and $\lfloor x \rfloor$ as the floor function, where $\lfloor x \rfloor = \max\{m \in \mathbb{Z} \mid m \leq x\}$.

We note that, when the exact solution of the original nonlinear reaction term is difficult to obtain, the nonlinear equation can be rewritten into a form with a known analytical solution while keeping the main features of the original dynamics. By using a frozen-coefficient method, the resulting equation can be solved efficiently at each time step without solving the original nonlinear problem directly. For example, the method in [26] replaces the original nonlinear reaction term with a locally equivalent form that has the same equilibrium structure and similar behavior. This approach allows efficient computation while preserving the accuracy of the solution.

For **Step 2**, the equation is discretized by the finite difference method as

$$\frac{\phi_{ij}^{**}-\phi_{ij}^{*}}{\Delta t}=2\epsilon\frac{\phi_{i-1,j}^{**}-2\phi_{ij}^{**}+\phi_{i+1,j}^{**}}{w_n^n h^2}-\frac{1}{2w_n^n}\sum_{p=1}^{n-1}w_p^n\frac{\phi_{ij}^{p+1}-\phi_{ij}^{p}}{\Delta t}. \tag{12}$$

Equation (12) can be rearranged into the form

$$\frac{2\epsilon}{h^2}\phi_{i-1,j}^{**}-(\frac{4\epsilon}{h^2}+\frac{w_n^n}{\Delta t})\phi_{ij}^{**}+\frac{2\epsilon}{h^2}\phi_{i+1,j}^{**}=-\frac{w_n^n}{\Delta t}\phi_{ij}^{*}+\frac{1}{2}\sum_{p=1}^{n-1}w_p^n\frac{\phi_{ij}^{p+1}-\phi_{ij}^{p}}{\Delta t}. \tag{13}$$

Furthermore, equation (13) can be cast into the standard tridiagonal form

$$a_i\phi_{i-1,j}^{**}+b_i\phi_{i,j}^{**}+c_i\phi_{i+1,j}^{**}=F_i, \tag{14}$$

where

$$a_i=\frac{2\epsilon}{h^2},\quad b_i=-\frac{4\epsilon}{h^2}-\frac{w_n^n}{\Delta t},\quad c_i=\frac{2\epsilon}{h^2},\quad F_i=-\frac{w_n^n}{\Delta t}\phi_{ij}^{*}+\frac{1}{2}\sum_{p=1}^{n-1}w_p^n\frac{\phi_{ij}^{p+1}-\phi_{ij}^{p}}{\Delta t}. \tag{15}$$

We enforce the zero Neumann boundary condition in the form:

$$\phi_{0j}=\phi_{1j},\quad \phi_{N_x+1j}=\phi_{N_xj},\quad \text{for}\quad j=1,2,\ldots,N_y. \tag{16}$$

Therefore, under the zero Neumann boundary condition, the coefficients at the boundary points are updated as

$$b_1=a_1+b_1=-\frac{2\epsilon}{h^2}-\frac{w_n^n}{\Delta t},\quad b_{N_x}=b_{N_x}+c_{N_x}=-\frac{2\epsilon}{h^2}-\frac{w_n^n}{\Delta t}.$$

The specific forms are as follows:

$$\begin{pmatrix} b_1 & c_1 & & & & \\ a_2 & b_2 & c_2 & & & \\ & a_3 & b_3 & c_3 & & \\ & & \ddots & \ddots & \ddots & \\ & & & a_{N_x-1} & b_{N_x-1} & c_{N_x-1} \\ & & & & a_{N_x} & b_{N_x} \end{pmatrix}\begin{pmatrix} \phi_1^{**} \\ \phi_2^{**} \\ \phi_3^{**} \\ \vdots \\ \phi_{N_x-1}^{**} \\ \phi_{N_x}^{**} \end{pmatrix}=\begin{pmatrix} F_1 \\ F_2 \\ F_3 \\ \vdots \\ F_{N_x-1} \\ F_{N_x} \end{pmatrix}. \tag{17}$$

Because the coefficient matrix is tridiagonal, the linear system can be solved efficiently by the Thomas algorithm [27].

For **Step 3**, we solve the equation using the finite difference method as follows:

$$\frac{\phi_{ij}^{n+1}-\phi_{ij}^{**}}{\Delta t}=2\epsilon\frac{\phi_{i,j-1}^{n+1}-2\phi_{ij}^{n+1}+\phi_{i,j+1}^{n+1}}{w_n^n h^2}-\frac{1}{2w_n^n}\sum_{p=1}^{n-1}w_p^n\frac{\phi_{ij}^{p+1}-\phi_{ij}^{p}}{\Delta t}. \tag{18}$$

Equation (18) can be rearranged into the form

$$\frac{2\epsilon}{h^2}\phi_{i,j-1}^{n+1} - \left(\frac{4\epsilon}{h^2} + \frac{w_n^n}{\Delta t}\right)\phi_{ij}^{n+1} + \frac{2\epsilon}{h^2}\phi_{i,j+1}^{n+1} = -\frac{w_n^n}{\Delta t}\phi_{ij}^{**} + \frac{1}{2}\sum_{p=1}^{n-1} w_p^n \frac{\phi_{ij}^{p+1} - \phi_{ij}^{p}}{\Delta t}. \tag{19}$$

Furthermore, equation (19) can be cast into the standard tridiagonal form

$$a_j\phi_{i,j-1}^{n+1} + b_j\phi_{i,j}^{n+1} + c_j\phi_{i,j+1}^{n+1} = F_j, \tag{20}$$

where

$$a_j = \frac{2\epsilon}{h^2}, \quad b_j = -\frac{4\epsilon}{h^2} - \frac{w_n^n}{\Delta t}, \quad c_j = \frac{2\epsilon}{h^2}, \; F_j = -\frac{w_n^n}{\Delta t}\phi_{ij}^{**} + \frac{1}{2}\sum_{p=1}^{n-1} w_p^n \frac{\phi_{ij}^{p+1} - \phi_{ij}^{p}}{\Delta t}. \tag{21}$$

The zero Neumann boundary condition is set as follows:

$$\phi_{i0} = \phi_{i1}, \quad \phi_{iN_y+1} = \phi_{iN_y}, \quad \text{for} \quad i = 1, 2, \ldots, N_x. \tag{22}$$

The coefficients at the boundary are updated as

$$b_1 = a_1 + b_1 = -\frac{2\epsilon}{h^2} - \frac{w_n^n}{\Delta t}, \quad b_{N_y} = b_{N_y} + c_{N_y} = -\frac{2\epsilon}{h^2} - \frac{w_n^n}{\Delta t}.$$

The specific forms are the same as those in equation (14).

3. Numerical experiments

3.1. Fitting of ϵ with respect to interface thickness

When $\phi^n = \phi^{n-1}$, the system reaches an equilibrium solution. In this study, we define the numerical equilibrium solution as follows: if the error measured in the L_∞-norm satisfies $\|\phi^n - \phi^{n-1}\|_\infty < \text{tol}$, then the state is considered a numerical equilibrium solution, where $\|\phi^n - \phi^{n-1}\|_\infty = \max_i \left|\phi_i^n - \phi_i^{n-1}\right|$. Here, tol is the preset tolerance, and in this study we take $\text{tol} = 10^{-6}$. We use linear interpolation to determine x_l and x_r that satisfy $\phi(x_l) = 0.05$ and $\phi(x_r) = 0.95$. The interface thickness is defined as $L = |x_r - x_l|$. The points x_l and x_r, as well as the interface thickness L, are illustrated in Figure 2. Under equilibrium conditions, we fit the relationship between ϵ and the interface thickness using a linear function, $\epsilon_\alpha(L) = aL + b$.

For different values of α, separate fittings are performed, where a and b are the fitting parameters. We apply the one-dimensional MM functional for the fitting. The domain is taken as $\Omega = (-1, 1)$ with $N_x = 256$, giving a spatial step size of $h = 2/N_x$. Here, we use the time step size $\Delta t = 0.01h^2$. The initial condition is specified as:

$$\phi(x, 0) = \begin{cases} 1, & x > 0 \\ 0, & x \le 0. \end{cases} \tag{23}$$

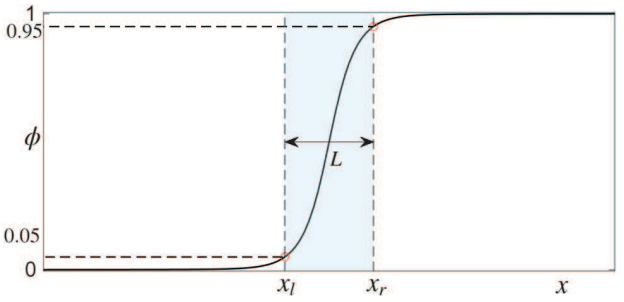

Figure 2. Schematic for interface thickness L.

Using the above algorithm, we obtain the following results.

$$\epsilon_{0.1} = 0.9966L - 0.0044, \epsilon_{0.2} = 0.9191L - 0.0043, \epsilon_{0.3} = 0.8836L - 0.0050,$$
$$\epsilon_{0.4} = 0.8659L - 0.0054, \epsilon_{0.5} = 0.8537L - 0.0056, \epsilon_{0.6} = 0.8434L - 0.0057,$$
$$\epsilon_{0.7} = 0.8348L - 0.0057, \epsilon_{0.8} = 0.8298L - 0.0058, \epsilon_{0.9} = 0.8398L - 0.0063,$$
$$\epsilon_{1.0} = 0.8861L - 0.0078.$$

3.2. Equilibrium test with different α

The computational domain is set as $\Omega = (-1, 1)$ with $N_x = 256$, and $h = 2/N_x$. Here, we use the parameter $L = 20h$, and the same ϵ is applied for all values of α. We will use two types of initial conditions to verify the equilibrium solution:

$$\phi(x, 0) = \begin{cases} 1, & x > 0 \\ 0, & x \le 0, \end{cases} \quad \text{and} \quad \phi(x, 0) = \frac{1}{2}(x + 1).$$

Figure 3 displays the equilibrium solutions under two different initial conditions, with $\alpha = 0.6, 0.8$, and 1. We observe that different initial conditions converge to the same equilibrium solution. Figure 3(d) illustrates the temporal evolution of the L_∞-norm error for three parameter values, $\alpha = 0.6$, 0.8, and 1.0. All curves show a rapid decay of the error at the initial stage, followed by a slower decrease, with slight variations among different α values.

3.3. Convergence rate

We examine the temporal convergence rate of the proposed normalized time-fractional MM scheme using the one-dimensional layered initial state

$$\phi(x, 0) = \frac{1}{4}\left[1 - \tanh\left(\frac{x + 0.6}{\eta}\right)\right] + \frac{1}{4}\left[1 - \tanh\left(\frac{x + 0.1}{\eta}\right)\right] + \frac{1}{4}\left[1 - \tanh\left(\frac{x - 0.1}{\eta}\right)\right] + \frac{1}{4}\left[1 - \tanh\left(\frac{x - 0.6}{\eta}\right)\right],$$

where $\eta = 0.04$. The computational domain is $\Omega = (-1, 1)$, $N_x = 32$, and $h = 2/N_x$. We set $T = 2.0 \times 10^{-3}$, $\Delta t = 10^{-4}$, and $\Delta t_{\text{ref}} = \Delta t/2^9$ for the

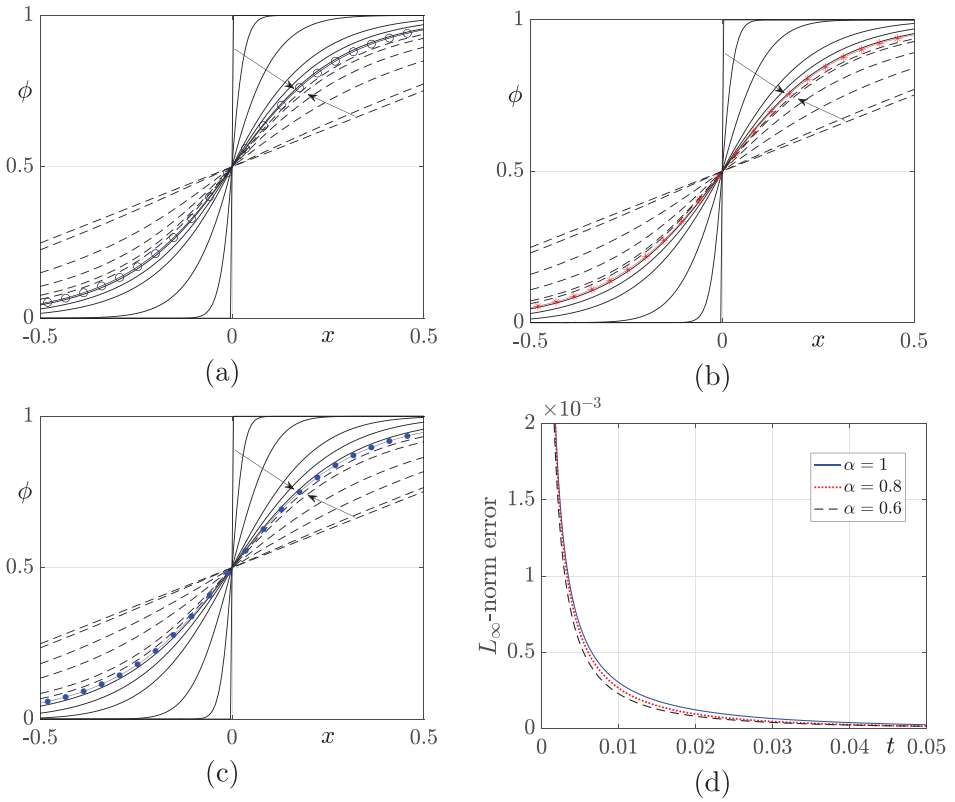

Figure 3. (a)–(c) depict the evolution of two different initial conditions with $\alpha = 0.6, 0.8$, and 1 toward the same equilibrium. (d) Evolution of the L_∞-norm error over time for $\alpha = 0.6, 0.8$, and 1.0, where the L_∞-norm error is defined as $\max_i \left|\phi_i^n - \phi_i^{n-1}\right|$.

Table 1. Discrete root-mean-square errors and convergence rates for the proposed method with fixed h and various Δt.

α	Δt	rate	$\Delta t/2$	rate	$\Delta t/4$	rate	$\Delta t/8$
0.8	1.3238e−4	1.04	6.4448e−5	1.04	3.1396e−5	1.04	1.5281e−5
0.9	1.4894e−4	1.03	7.2844e−5	1.04	3.5548e−5	1.04	1.7299e−5
1.0	1.8781e−4	0.99	9.4286e−5	1.00	4.7101e−5	1.01	2.3401e−5

reference solution. The parameter ϵ is chosen as $\epsilon = \epsilon_\alpha(4h)$ according to the fitted formulas in Section 3.1. The error is computed by the discrete root-mean-square norm

$$E_{\Delta t} = \left(\frac{1}{N_x} \sum_{i=1}^{N_x} \left| \phi_i^{\Delta t}(T) - \phi_i^{\text{ref}}(T) \right|^2 \right)^{1/2}.$$

The temporal convergence rate is defined as $\log_2(E_{\Delta t}/E_{\Delta t/2})$. Table 1 reports the errors and convergence rates for $\alpha = 0.8, 0.9$, and 1.0. The results show that the proposed method achieves approximately first-order temporal convergence.

We next test the spatial convergence for $\alpha = 0.8$ using the same initial condition. To isolate the spatial discretization error, we fix $\epsilon = \epsilon_{0.8}(4h)$, where

Table 2. Discrete root-mean-square errors and spatial convergence rates for $\alpha = 0.8$.

h	error	rate	$h/2$	error	rate	$h/4$	error
3.1250e−2	1.4952e−3	2.01	1.5625e−2	3.7146e−4	2.00	7.8125e−3	9.2668e−5

$h = 1/32$. We set $T = 2.0 \times 10^{-3}$ and $\Delta t = 10^{-4}$, and use $N_x = 64, 128, \ldots, 1024$. Using the coarse–fine grid comparison, the error between the numerical solutions on grids with $N_x = N$ and $N_x = 2N$ is computed by

$$E_N = \left(\frac{1}{N} \sum_{i=1}^{N} \left| \Phi_i(T) - \frac{\phi_{2i-1}(T) + \phi_{2i}(T)}{2} \right|^2 \right)^{1/2},$$

where Φ_i denotes the coarse-grid solution and ϕ_i denotes the fine-grid solution. The spatial convergence rate is defined as $\log_2(E_N/E_{2N})$. Table 2 shows that the proposed finite-difference discretization achieves approximately second-order spatial accuracy.

3.4. Comparison with Caputo derivative

The Caputo fractional derivative is one of the most commonly used definitions in time-fractional models. It is defined as

$$\frac{\partial^\beta \phi(\mathbf{x}, t)}{\partial t^\beta} = \frac{1}{\Gamma(1-\beta)} \int_0^t \frac{\partial \phi(\mathbf{x}, s)}{\partial s} \frac{ds}{(t-s)^\beta}, \quad 0 < \beta < 1. \tag{25}$$

In the two-dimensional computational domain $\Omega = (-1, 1)^2$, the discretization is performed with $N_x = N_y = 128$ and a uniform spatial step size $h = 2/N_x$. Unless otherwise stated, different values of ϵ are used for different time-fractional orders, with their magnitudes taken from the results shown in 3.1. We use $\epsilon = \epsilon_\alpha(8h)$. The time step is taken as $\Delta t = 2h^2$. The initial condition is specified as

$$\phi(x, y, 0) = \frac{1}{2} \left[\tanh\left(\frac{0.5 - \sqrt{x^2 + y^2}}{\sqrt{2}\,\epsilon} \right) + 1 \right], \quad -1 \le x \le 1, \quad -1 \le y \le 1.$$

Figure 4(a) and (b) illustrate the evolution of the numerical radius over time under the normalized and Caputo derivatives, respectively. In the normalized case, the results are presented for $\alpha = 0.6, 0.8$, and 1, while in the Caputo case, they are shown for $\beta = 0.6, 0.8$, and 1. The numerical radius is defined as the average distance from the center to the points on the 0.5 level contour. Compared with the Caputo derivative, the normalized derivative model produces a smoother temporal evolution. Moreover, for different fractional orders, the variations under the normalized model are relatively smaller, exhibiting lower sensitivity to changes in the fractional order. This property helps maintain consistency and predictability in practical computations.

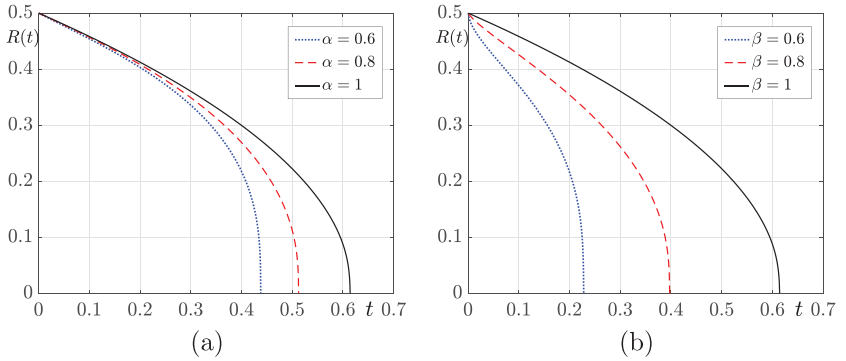

Figure 4. Comparison of the evolution of the numerical radius $R(t)$ under the normalized (a) and caputo (b) derivatives for different fractional orders. The normalized case is computed for $\alpha = 0.6, 0.8$, and 1, while the caputo case is shown for $\beta = 0.6, 0.8$, and 1.

To examine the energy variation in the normalized time-fractional MM model, we also compute the discrete energy for the case $\alpha = 0.8$. The computational domain, mesh, and initial condition are the same as those used in Figure 4. In this test, $N_x = N_y = 128$, $h = 2/N_x$, $\Delta t = 2h^2$, and the final time is $T = 0.5$. We set $m = 8$ and use the fitted interfacial parameter

$$\epsilon = \epsilon_{0.8}(8h) = 0.8298(8h) - 0.0058.$$

The discrete energy is defined as follows:

$$\mathcal{E}_h(\phi^n) = h^2 \left[\epsilon \sum_{i=1}^{N_x-1} \sum_{j=1}^{N_y} \left(\frac{\phi^n_{i+1,j} - \phi^n_{ij}}{h} \right)^2 + \epsilon \sum_{i=1}^{N_x} \sum_{j=1}^{N_y-1} \left(\frac{\phi^n_{i,j+1} - \phi^n_{ij}}{h} \right)^2 + \frac{1}{\epsilon} \sum_{i=1}^{N_x} \sum_{j=1}^{N_y} \sin^2(\pi \phi^n_{ij}) \right]. \tag{26}$$

As shown in Figure 5, the discrete energy decreases monotonically with time, which confirms the energy-dissipative nature of the normalized time-fractional MM model.

3.5. Motion by mean curvature

In the domain $\Omega = (-1, 1)^2$, we use $N_x = N_y = 128$ and $h = 2/N_x = 2/N_y$ for the uniform spatial discretization. The initial condition $\phi(x, y, 0)$ consists of several smooth circular interfaces of different sizes, each described by a

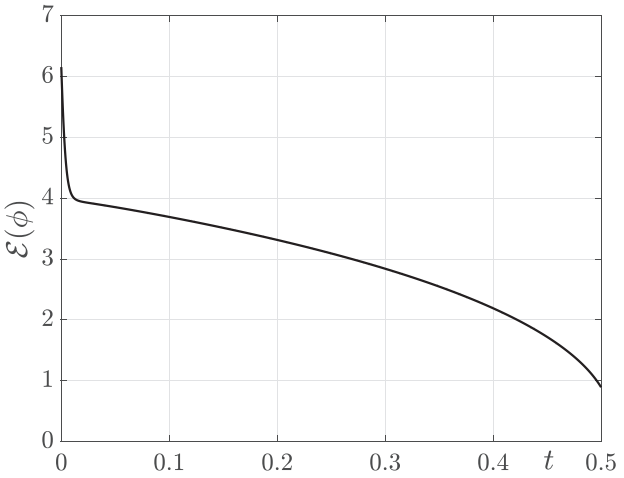

Figure 5. Energy evolution of the normalized time-fractional MM model for $\alpha = 0.8$.

hyperbolic tangent function. The initial condition is specified as follows:

$$\phi(x,y,0) = \begin{cases} \frac{1}{2}\left[\tanh\left(\frac{0.1-\sqrt{(x-\frac{1}{3})^2+(y-0.5)^2}}{0.02}\right)+1\right] \\ +\frac{1}{2}\left[\tanh\left(\frac{0.225-\sqrt{(x-\frac{1}{3})^2+(y+0.5)^2}}{0.02}\right)+1\right], & -1\le x<-\frac{1}{3}, \quad -1\le y\le 1, \\ 1+\frac{1}{2}\left[\tanh\left(\frac{0.125-\sqrt{x^2+(y-0.5)^2}}{0.02}\right)+1\right] \\ +\frac{1}{2}\left[\tanh\left(\frac{0.2-\sqrt{x^2+(y+0.5)^2}}{0.02}\right)+1\right], & -\frac{1}{3}\le x<\frac{1}{3}, \quad -1\le y\le 1, \\ 2+\frac{1}{2}\left[\tanh\left(\frac{0.15-\sqrt{(x+\frac{1}{3})^2+(y-0.5)^2}}{0.02}\right)+1\right] \\ +\frac{1}{2}\left[\tanh\left(\frac{0.175-\sqrt{(x+\frac{1}{3})^2+(y+0.5)^2}}{0.02}\right)+1\right], & \frac{1}{3}\le x\le 1, \quad -1\le y\le 1. \end{cases}$$

These circular interfaces are distributed across three step-like regions arranged along the x-direction, with the background value increasing progressively from one region to the next, thus forming a layered initial structure. Figure 6(a) illustrates the initial condition. The numbers labeled in the Figure 6(a) indicate the sequence in which the interfaces gradually shrink and eventually vanish over time. We use the time step $\Delta t = 0.5h^2$. Here, we use $\epsilon = \epsilon_\alpha(6h)$. Figure 6 shows snapshots at $t = 580\Delta t$ for different fractional orders $\alpha = 0.4, 0.8, 1$. We adopt the numbering from Figure 6(a) to ensure consistency in the description. In Figure 6(b) ($\alpha = 0.4$), the interface labeled 5 has significantly shrunk and almost completely vanished, leaving only a faint trace. In Figure 6(c) ($\alpha = 0.8$), the interface 5 appears wider and more pronounced compared to Figure 6(b), while the interface 6 exhibits a slight but noticeable protrusion. For Figure 6(d) ($\alpha = 1.0$), the interface 6 remains clear and well-defined.

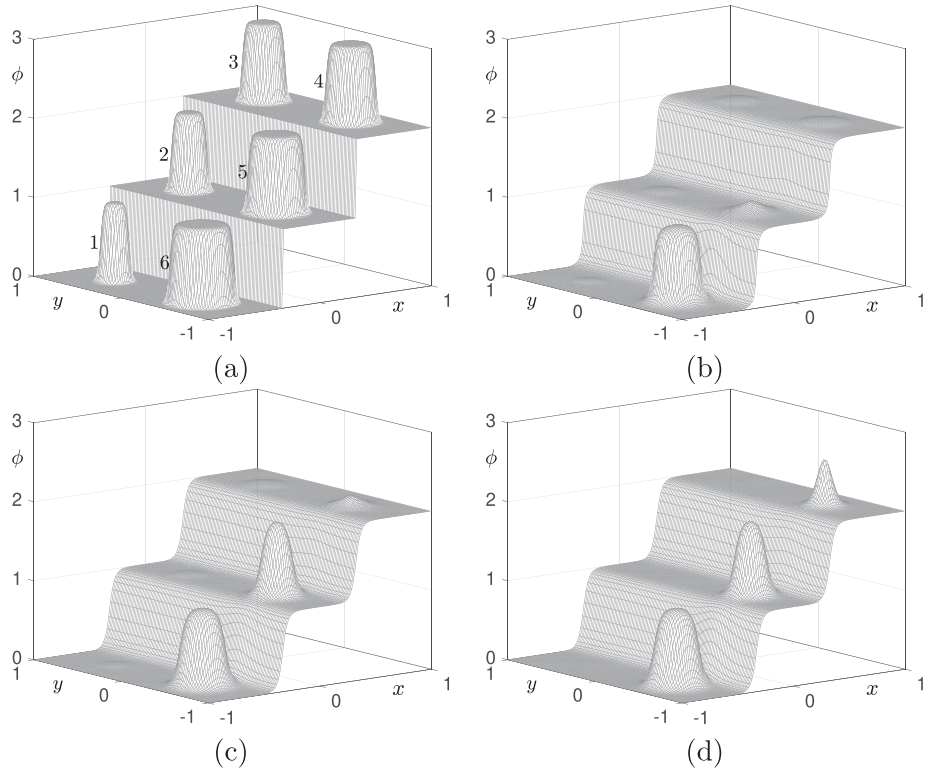

Figure 6. Snapshot of initial condition (a) and snapshots at $t = 580\Delta t$ for different fractional orders: (b) $\alpha = 0.4$, (c) $\alpha = 0.8$, and (d) $\alpha = 1.0$. The time step is $\Delta t = 0.5h^2$.

This difference reflects the sensitivity of the normalized time derivative to the fractional order, indicating that smaller α values accelerate the interface shrinkage while larger α values slow down its evolution.

On the computational domain $\Omega = (-1, 1)^2$, we use a uniform mesh with $N_x = N_y = 128$. The time step is $\Delta t = 0.5h^2$. We use $\epsilon = \epsilon_\alpha(6h)$. The initial condition is given by

$$\phi(x, y, 0) = \sum_{k=1}^{3} \frac{1}{2}\left[1 + \tanh\left(\frac{r_k - r^*(x, y)}{\varepsilon}\right)\right], \quad -1 \le x \le 1, \quad -1 \le y \le 1, \tag{27}$$

where

$$r^*(x, y) = r\,(1 + 0.3\cos(5\theta))\,, \quad r = \sqrt{x^2 + y^2}, \quad \theta = \arctan\left(\frac{y}{x}\right).$$

Here, we use the parameter values $r_1 = 0.6, r_2 = 0.4, r_3 = 0.2$. Figure 7(c) shows the initial condition, while Figure 7(d) and (e) show snapshots at $t = 1000\Delta t$ for $\alpha = 0.4$ and $\alpha = 1$, respectively. Figure 7(a) displays the contours at levels 0.5, 1.5, and 2.5 for the initial condition, corresponding to the red, blue, and black lines, respectively. Figure 7(b) shows the contours at levels 0.5,

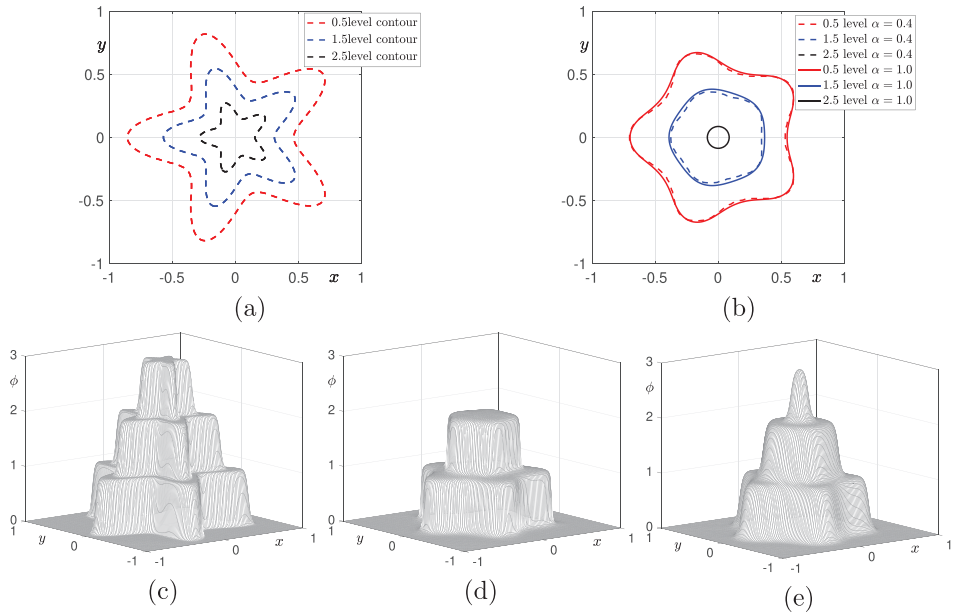

Figure 7. (a) Contours for the initial condition at levels 0.5, 1.5, and 2.5, shown as red, blue, and black lines, respectively. (b) Contours at levels 0.5, 1.5, and 2.5 for $\alpha = 0.4$ and $\alpha = 1$. (c) The initial condition. (d) Snapshot at $t = 1000\Delta t$ for $\alpha = 0.4$. (e) snapshot at $t = 1000\Delta t$ for $\alpha = 1$.

1.5, and 2.5 for $\alpha = 0.4$ and $\alpha = 1$. From this experiment, we obtain the same conclusion as in the previous one, namely that a smaller α accelerates the temporal evolution. In Figure 7(b), for $\alpha = 0.4$, the contour at level 0.5 has already completely disappeared, whereas it still exists for $\alpha = 1$. Moreover, the star-shaped structure is better preserved for smaller α, while larger α leads to smoother and more rounded contours. By observing Figure 7(d) and (e), we can also see that the transition of the phase-field surface becomes steeper for smaller α.

3.6. Stability test

We investigate the stability of the proposed scheme under a random initial profile in two dimensions. The computational domain is taken as $\Omega = (0, 1)^2$ with $N_x = N_y = 128$, and the spatial step size is $h = 1/N_x$. We set $m = 5$ and use the interfacial parameter $\epsilon = 0.61405mh$. We use the same initial condition as in equation (27). To compare the stability behavior under different time step sizes while keeping the same final time, we consider three cases. The first uses a time step size of $10h^2$ with 50 time steps, the second uses a time step size of h^2 with 500 time steps, and the third uses a time step size of $0.1h^2$ with 5000 time steps. Thus all three tests have the same final time T. Figure 8 shows the random initial condition and the numerical solutions obtained with the three choices of Δt.

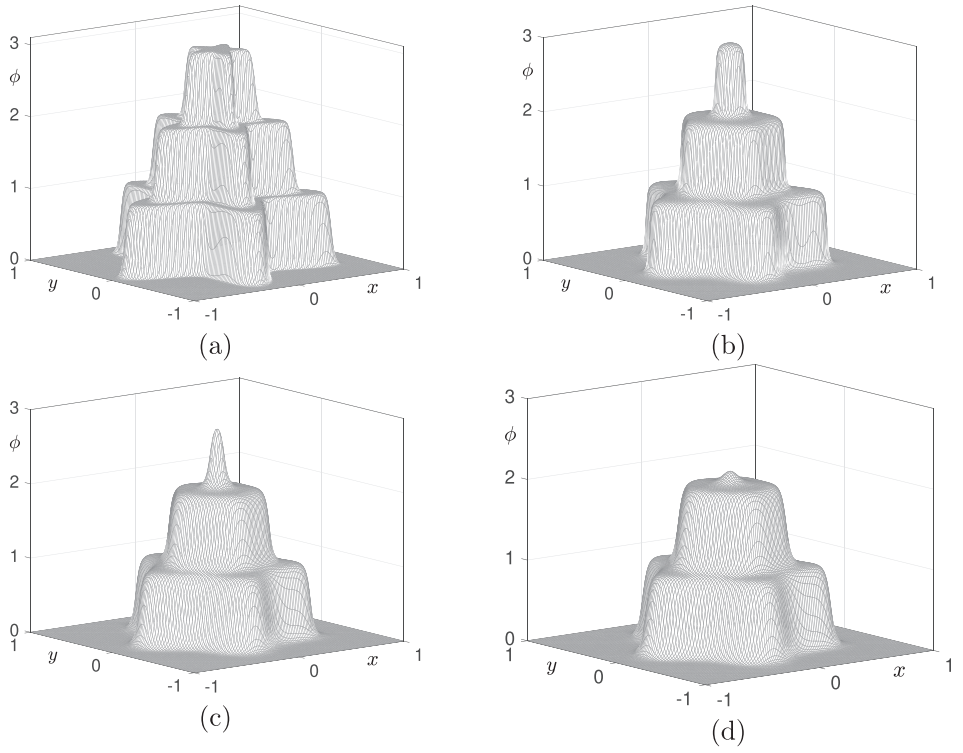

Figure 8. Stability test. (a) Initial condition. (b) Numerical solution with $\Delta t = 10h^2$ and $N_t = 50$. (c) numerical solution with $\Delta t = h^2$ and $N_t = 500$. (d) numerical solution with $\Delta t = 0.1h^2$ and $N_t = 5000$.

3.7. Time-fractional MM functional with advection term

The governing equation with an additional advection term is given by

$$\frac{\partial^\alpha \phi(\mathbf{x},t)}{\partial t^\alpha} + \nabla\cdot(\phi(\mathbf{x},t)\mathbf{u}(\mathbf{x},t)) = -\frac{\pi}{\epsilon}\sin\left(2\pi\phi(\mathbf{x},t)\right) + 2\epsilon\Delta\phi(\mathbf{x},t), \quad (28)$$

where $\mathbf{u}(\mathbf{x},t)$ denotes the imposed flow field. The convection term in equation (28) is discretized as

$$\mathcal{A}_{ij}^n := \nabla\cdot\left(\phi_{ij}^n\mathbf{u}_{ij}^n\right) = \frac{(\phi_{i+1,j}^n+\phi_{ij}^n)u^n_{i+\frac{1}{2},j} - (\phi_{ij}^n+\phi_{i-1,j}^n)u^n_{i-\frac{1}{2},j}}{2h} + \frac{(\phi_{i,j+1}^n+\phi_{ij}^n)v^n_{i,j+\frac{1}{2}} - (\phi_{ij}^n+\phi_{i,j-1}^n)v^n_{i,j-\frac{1}{2}}}{2h}. \quad (29)$$

The background swirling flow $\mathbf{u}(\mathbf{x},t) = (u(x,y,t), v(x,y,t))$ is chosen as

$$u(x,y,t) = 2\sin^2(\pi x)\sin(2\pi y), \quad (30)$$

$$v(x,y,t) = -2\sin^2(\pi y)\sin(2\pi x). \quad (31)$$

We consider the domain $\Omega = (0,2)\times(0,1)$. Here, we set $N_x = 256$ and $N_y = 128$. Then, $h = 1/128$ and $\Delta t = 2h^2$. We use $\epsilon = \epsilon_\alpha(8h)$. To solve

equation (28) numerically, we apply the OSM, expressed as:

$$\textbf{Step 1:}\quad \frac{\partial \phi(x_i, y_j, t_{n+1})}{\partial t} = -\frac{\pi \sin(2\pi(\phi(x_i, y_j, t_{n+1})))}{w_n^n \epsilon}. \tag{32}$$

$$\textbf{Step 2:}\quad \frac{\partial \phi(x_i, y_j, t_{n+1})}{\partial t} + \frac{1}{2w_n^n}\mathcal{A}_{ij}^n = \frac{2\epsilon}{w_n^n}\phi_{xx}(x_i, y_j, t_{n+1}) - \frac{1}{2w_n^n}\sum_{p=1}^{n-1} w_p^n \frac{\phi_{ij}^{p+1} - \phi_{ij}^p}{\Delta t}. \tag{33}$$

$$\textbf{Step 3:}\quad \frac{\partial \phi(x_i, y_j, t_{n+1})}{\partial t} + \frac{1}{2w_n^n}\mathcal{A}_{ij}^n = \frac{2\epsilon}{w_n^n}\phi_{yy}(x_i, y_j, t_{n+1}) - \frac{1}{2w_n^n}\sum_{p=1}^{n-1} w_p^n \frac{\phi_{ij}^{p+1} - \phi_{ij}^p}{\Delta t}. \tag{34}$$

The initial condition $\phi(x, y, 0)$ is defined as follows:

$$\phi(x, y, 0) = \begin{cases} \frac{1}{2}\left[\tanh\left(\frac{0.25 - \sqrt{(x-0.5)^2 + (y-0.7)^2}}{0.01\sqrt{2}}\right) + 1\right], & 0 < x \le 1, \\ 1 + \frac{1}{2}\left[\tanh\left(\frac{0.2 - \sqrt{(x-1.5)^2 + (y-0.7)^2}}{0.01\sqrt{2}}\right) + 1\right], & 1 < x \le 2. \end{cases} \tag{35}$$

Figure 9 presents the time evolution of two droplets under the imposed swirling flow field for different values of α. The contours at $\phi = 0.5$ (red) and $\phi = 1.5$ (blue) are plotted at $t = 200\Delta t$, $800\Delta t$, and $1200\Delta t$. At the early stage, the droplets begin to shift and stretch under the swirling flow. The left droplet (red contour) gradually drifts downward and rightward, while the right droplet (blue contour) is displaced toward the lower-left direction. Different α values result in distinct evolution rates: for $\alpha = 0.6$, the contour contracts more rapidly and the droplet size decreases significantly. In contrast, for $\alpha = 0.8$ and $\alpha = 1.0$, the contours retain larger areas and exhibit slower positional changes. At the intermediate stage, the droplets are further stretched by the background flow. The red contour shows that the left droplet is elongated toward the right, while the blue contour of the right droplet shrinks and shifts leftward. When $\alpha = 0.6$, the droplet area reduces more quickly and its displacement is more pronounced. By comparison, for $\alpha = 0.8$ and $\alpha = 1.0$, the droplet maintains a relatively larger size and evolves more slowly. At the later stage, the differences among α values become more significant. For $\alpha = 0.6$, the left droplet (red contour) shows substantial reduction in size and stronger displacement, while the right droplet leaves only a small remaining contour. On the other hand, for $\alpha = 0.8$ and $\alpha = 1.0$, the droplets preserve larger areas and more complete

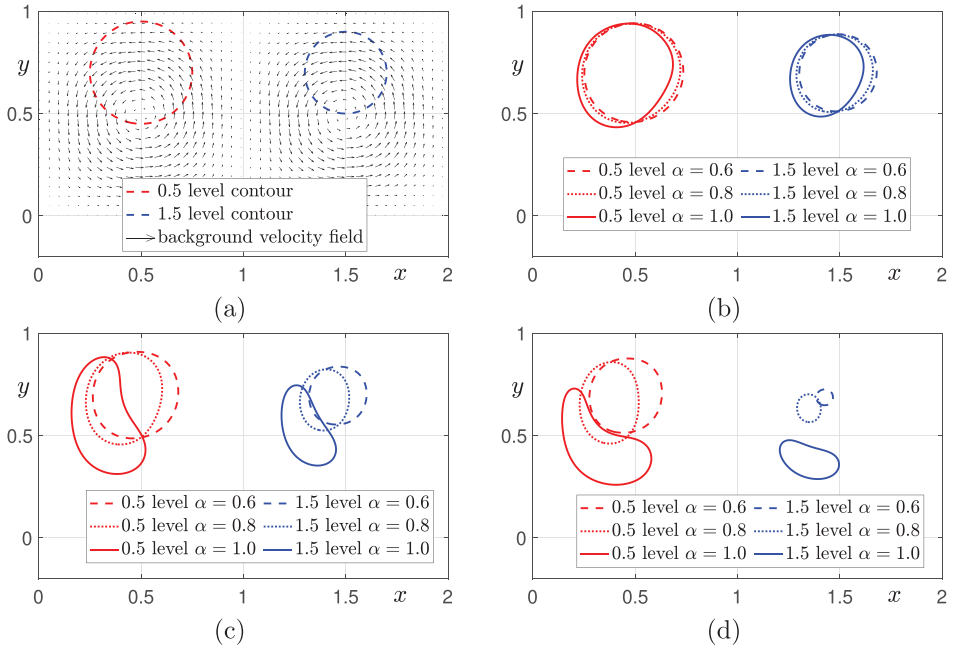

Figure 9. (a) The contours at the 0.5 and 1.5 levels of the initial condition, along with the background velocity field. (b), (c), and (d) show the contours at times $t = 200\Delta t$, $800\Delta t$, and $1200\Delta t$, respectively, for $\alpha = 0.6, 0.8$, and 1.0. The red lines represent the 0.5 level contour, and the blue lines represent the 1.5 level contour.

contours, with slower displacement compared to the smaller α case. Overall, the parameter α primarily influences the droplet evolution rate and the contour size. Smaller α values (e.g., $\alpha = 0.6$) accelerate the contraction of the droplet area and lead to faster positional shifts, indicating a faster evolution. In contrast, larger α values ($\alpha = 0.8, 1.0$) allow the droplets to maintain larger sizes and slower displacements, corresponding to a slower evolution rate.

4. Conclusions

In this paper, we propose a normalized time-fractional gradient flow model of the MM functional, along with a numerical algorithm that combines operator splitting and finite difference methods. The key feature of the proposed method lies in the use of an analytical solution for the nonlinear reaction term, which effectively captures the memory effects in fractional dynamics. Through numerical tests, we verify the stability of the method under different initial conditions and systematically examine the influence of the fractional order on the interfacial evolution process. The results demonstrate that the fractional order can regulate interfacial dynamics. It also provides an additional degree of freedom in modeling. Moreover, the proposed normalized time-fractional MM functional model offers a numerical tool for multiphase simulations. The method may have broad applications in fractional phase-field models. Future work will extend the

method to more complex geometries and three-dimensional problems. We will also study its applications in multiphysics-coupled phase-field models.

Author contributions

CRediT: **Zhengang Li**: Resources, Software, Visualization, Writing – original draft, Writing – review & editing; **Soobin Kwak**: Resources, Software, Visualization, Writing – original draft, Writing – review & editing; **Xinpei Wu**: Resources, Software, Visualization, Writing – original draft, Writing – review & editing; **Juho Ma**: Resources, Software, Visualization, Writing – original draft, Writing – review & editing; **Qunzhi Jin**: Resources, Software, Visualization, Writing – original draft, Writing – review & editing; **Junseok Kim**: Resources, Software, Visualization, Writing – original draft, Writing – review & editing.

Disclosure statement

The authors declare that they have no conflicts of interest.

Funding

The corresponding author (J.S. Kim) was supported by the Brain Korea 21 FOUR from the Ministry of Education of Korea.

Data availability statement

No data were used for the research described in the article.

References

[1] Hakimzadeh, M., Mora-Corral, C., Walkington, N., Buscarnera, G., Dayal, K. (2026). Phase-field modeling of fracture under compression and confinement in anisotropic geomaterials. *Num. Anal. Meth. Geomechanics*. 50(1):369–386. DOI: 10.1002/nag.70101.

[2] Liu, N., Chen, M. W., Zhang, M., Wang, Z. (2024). Morphological evolution of particles in alloy melts during initial crystal growth: Insights from phase field simulations. *Physica B*. 688:416133. DOI: 10.1016/j.physb.2024.416133.

[3] Cai, T., Wang, G., Qiu, Z., Zheng, Z., Zeng, D., Bai, C., Xiao, N. (2025). Exploring the effects of solution temperature and cooling rate on α phase in a multicomponent titanium alloy: Insights from phase-field simulations. *J. Alloys Compd.* 1010:177318. DOI: 10.1016/j.jallcom.2024.177318.

[4] Xia, B., Lai, S., Xia, Q., Liu, X., Li, Y., Kim, J. (2025). Phase-field modeling of fiber-based thermal diffusion and phase transitions in the fused deposition modeling process. *Commun. Nonlinear Sci. Numer. Simul.* 151:109071. DOI: 10.1016/j.cnsns.2025.109071.

[5] Dolai, A. K., Pandey, V., Biswas, G., Chakraborty, S. (2025). A hybrid phase field-volume of fluid method for simulating dynamically evolving interfaces in multiphase flows. *Comput. Fluids*. 289:106536. DOI: 10.1016/j.compfluid.2024.106536.

[6] Xiao, Y., Zeng, Z., Zhang, L., Wang, J., Wang, Y., Huang, C. (2024). A reduction-consistent phase field model for non-isothermal multiphase flows of

N immiscible incompressible fluids. *Int. J. Heat Mass Transf.* 228:125657. DOI: 10.1016/j.ijheatmasstransfer.2024.125657.

[7] Rath, B., Mao, X., Jaiman, R. K. (2024). An efficient phase-field framework for contact dynamics between deformable solids in fluid flow. *Comput. Methods Appl. Mech. Eng.* 432:117348. DOI: 10.1016/j.cma.2024.117348.

[8] Wang, Z., Xie, W., Kim, J., Li, Y. (2026). A modified ensemble Kalman filter method with an adaptive ensemble strategy for multiphase flow systems. *J. Comput. Phys.* 561:114972. DOI: 10.1016/j.jcp.2026.114972.

[9] Lai, S., Feng, J., Lv, Z., Kim, J., Li, Y. (2025). A dual-energy physics-informed multi-material topology optimization method within the phase-field framework. *Comput. Methods Appl. Mech. Eng.* 447:118338. DOI: 10.1016/j.cma.2025.118338.

[10] Li, Y., Lv, Z., Xia, Q. (2025). On the unconditionally stable phase field model of ternary components system considering liquid-solid phase transition. *J. Comput. Phys.* 543:114404. DOI: 10.1016/j.jcp.2025.114404.

[11] Xia, B., Wang, K., Nam, Y., Li, Z., Wu, X., Kwak, S., Ma, J., Kim, J. (2026). Numerical analysis of the Allen–Cahn equation on non-uniform cell sizes. *Comput. Appl. Math.* 45:161.

[12] Giga, Y., Okamoto, J., Uesaka, M. (2023). *A finer singular limit of a single-well Modica–Mortola functional and its applications to the Kobayashi–Warren–Carter energy*. *Adv. Calc. Var.* 16(1):163–182. DOI: 10.1515/acv-2020-0113.

[13] Jafari, H., Malidareh, B. F., Hosseini, V. R. (2024). Collocation discrete least squares meshless method for solving nonlinear multi-term time fractional differential equations. *Eng. Anal. Bound. Elem.* 158:107–120. DOI: 10.1016/j.enganabound.2023.10.014.

[14] Bilal, M., Iqbal, J., Shah, K., Abdalla, B., Abdeljawad, T., Ullah, I. (2024). Analytical solutions of the space-time fractional Kundu–Eckhaus equation by using modified extended direct algebraic method. *Partial Differ. Equ. Appl. Math.* 11:100832. DOI: 10.1016/j.padiff.2024.100832.

[15] Baharlouei, S., Mokhtari, R. (2023). A stable and convergent hybridized discontinuous Galerkin method for time-fractional telegraph equations. *Numer. Funct. Anal. Optim.* 44(11):1175–1193. DOI: 10.1080/01630563.2023.2236690.

[16] Postavaru, O. (2025). Solving inverse problems for nonlinear fractional differential equations using fractional-order hybrid Fibonacci functions. *Numer. Funct. Anal. Optim.* 46(8–9):705–724. DOI: 10.1080/01630563.2025.2525313.

[17] Sohaib, M., Shah, A., Furati, K. M., Khaliq, H. (2025). A numerical scheme for time-fractional Allen–Cahn equation with application in phase separation. *Int. J. Comput. Math.* 102(3):449–464. DOI: 10.1080/00207160.2024.2420681.

[18] Jiang, H., Hu, D., Huang, H., Liu, H. (2024). Linearly implicit schemes preserve the maximum bound principle and energy dissipation for the time-fractional Allen–Cahn equation. *J. Sci. Comput.* 101(2):25. DOI: 10.1007/s10915-024-02667-2.

[19] Zhang, H., Liao, H. L. (2024). High-order energy stable variable-step schemes for the time-fractional Cahn–Hilliard model. *Math. Comput. Simul.* 223:171–182. DOI: 10.1016/j.matcom.2024.04.005.

[20] Wang, F., Chen, H., Wang, H. (2019). Finite element simulation and efficient algorithm for fractional Cahn–Hilliard equation. *J. Comput. Appl. Math.* 356:248–266. DOI: 10.1016/j.cam.2019.01.037.

[21] Lee, C., Nam, Y., Bang, M., Ham, S., Kim, J. (2024). Numerical investigation of the dynamics for a normalized time-fractional diffusion equation. *MATH*. 9(10):26671–26687. DOI: 10.3934/math.20241297.

[22] Wang, J., Liu, Q., Chen, K., Yang, J., Han, Z., Kwak, S., Nam, Y., Ham, S., Kim, J. (2025). An efficient operator splitting method for a normalized time-fractional Allen–Cahn equation. *Fractals*. 33(09):2550085. DOI: 10.1142/S0218348X25500859.

[23] Lee, H. G., Kwak, S., Ham, S., Hwang, Y., Kim, J. (2025). The normalized time-fractional Cahn–Hilliard equation. *Chaos. Solitons Fractals*. 198:116450. DOI: 10.1016/j.chaos.2025.116450.

[24] Ma, J., Kim, J. (2026). Numerical analysis of a normalized time-fractional Lorenz system. *Int. J. Bifurcat. Chaos*. 36(8):2650098.

[25] Ham, S., Kwak, S., Lee, C., Lee, G., Kim, J. (2023). A second-order time-accurate unconditionally stable method for a gradient flow for the Modica–Mortola functional. *J. Sci. Comput*. 95(2):63. DOI: 10.1007/s10915-023-02198-2.

[26] Yang, J., Kim, S., Kim, J. (2025). Unconditionally maximum principle preserving scheme for the Allen–Cahn equation with a logarithmic free energy. *Comput. Math. Appl*. 195:366–375. DOI: 10.1016/j.camwa.2025.07.032.

[27] Kwak, S. (2025). Practical implementation of boundary conditions in the Thomas algorithm. *J. Korean Soc. Ind. Appl. Math*. 29(2):171–183.